Thermometric investigations for the characterization of fatigue crack initiation and propagation in Wire and Arc Additively Manufactured parts with as-built surfaces

Lorenzo Bercelli, Cédric Doudard, S. Calloch, V. Le Saux, Julien Beaudet

▶ **To cite this version:**

Lorenzo Bercelli, Cédric Doudard, S. Calloch, V. Le Saux, Julien Beaudet. Thermometric investigations for the characterization of fatigue crack initiation and propagation in Wire and Arc Additively Manufactured parts with as-built surfaces. Fatigue and Fracture of Engineering Materials and Structures, 2023, 46 (1), pp.153-170. 10.1111/ffe.13854 . hal-03826772

HAL Id: hal-03826772

https://ensta-bretagne.hal.science/hal-03826772v1

Submitted on 9 Jun 2023

HAL is a multi-disciplinary open access archive for the deposit and dissemination of scientific research documents, whether they are published or not. The documents may come from teaching and research institutions in France or abroad, or from public or private research centers.

L'archive ouverte pluridisciplinaire **HAL**, est destinée au dépôt et à la diffusion de documents scientifiques de niveau recherche, publiés ou non, émanant des établissements d'enseignement et de recherche français ou étrangers, des laboratoires publics ou privés.

Thermometric investigations for the characterization of fatigue crack initiation and propagation in Wire and Arc Additively Manufactured parts with as-built surfaces

Lorenzo Bercelli[1] *, Cédric Doudard[1], Sylvain Calloch[1], Vincent Le Saux[1], Julien Beaudet[2]

[1] ENSTA Bretagne, IRDL - UMR CNRS 6027, 29200 Brest, France
[2] Naval Group Research, Technocampus Océan, 5 rue de l'Halbrane, 44340 Bouguenais, France

Abstract

Metal Additive Manufacturing (AM) allows for the fabrication of complex shapes with high added value at low costs. Indeed, as-built structures are near net shape : they require few to no finishing operations. However, as-built AM parts present significant roughness caused by the layer discretization. In the case of the Wire and Arc Additive Manufacturing (WAAM) process, used for large-scale structures, the as-built roughness is estimated to several hundreds of micrometers. For complex geometries, a complete machining of the surfaces is not necessarily possible. In this study, an experimental method is proposed, relying on thermoelastic stress analysis, to characterize the effect of as-built WAAM surface roughness on high-cycle fatigue properties. Using an infrared camera, multiple cracks can be detected and monitored over a large surface on rough WAAM samples under cyclic bending. The collected data constitutes valuable information for the identification of a fatigue model dedicated to as-built WAAM structures.

$Keywords$: Wire and Arc Additive Manufacturing (WAAM) ; High cycle fatigue ; Rough surface ; Thermoelastic Stress Analysis (TSA) ; Fracture mechanics

Nomenclature

A_l	Amplitude of the signal determined by the lock-in method
I_{1_a}	Amplitude of the stress tensor's first invariant
$\overline{R_a^{x,z}}$	Arithmetic average height roughness averaged on a surface for profiles perpendicular to the building direction and along the building direction, respectively
R_a	Arithmetic average height roughness
b	Basquin law's exponent
B	Basquin law's factor
$\sigma_{a_{nom}}$	Bending stress amplitude at the skin of a flat sample of thickness t_{nom}
α'	Coefficient of thermal expansion
$K^{0,-90}$	Correlation function of the lock-in method at a $0°$ or $-90°$ phase
a	Crack half-length
$A_{\%}$	Deformation to failure
ρ	Density
$\Delta\theta^c_{the_a}$	Differentiel of the temperature amplitude linked to the thermoelastic coupling measured by infrared camera
Δ	Dissipation heat source

$Abbreviations$: AM: Additive Manufacturing, DED: Direct Energy Deposition, SLM: Selective Laser Melting, TSA: Thermoelastic Stress Analysis, WAAM: Wire and Arc Additive Manufacturing

*Corresponding author. E-mail address: lorenzo.bercelli@ensta-bretagne.fr

$\mathscr{F}$	Fourier number
T_0	Initial temperature
R	Load ratio
R_v	Maximum depth of valleys of the roughness profile
R_t	Maximum height of the roughness profile
f_m	Mechanical loading frequency
t_{nom}	Median parallelepipedal shell thickness of as-built WAAM samples
t_{build}	Minimum containing parallelepipedal shell thickness of the as-built WAAM samples
N_P	Number of cycles in a sampled signal
N_r	Number of cycles to failure
N	Number of cycles
n	Number of sampled values in a signal cycle
m_p	Paris law's exponent
C_p	Paris law's factor
Φ_l	Phase of the signal determined by the lock-in method
$S^{0,-90}$	Sinusoidal projections of a signal at a $0°$ or $-90°$ phase according to the lock-in method
Z_t	Size of a pixel neighbourhood for the local thresholding method
c	Specific heat capacity
θ_d	Stabilized temperature rise of a sample under constant amplitude cyclic loading
K_{t_I}	Stress concentration factor in the sense of the stress tensor's first invariant
K_t	Stress concentration factor
ΔK	Stress intensity factor range
$\theta^c_{the_a}$	Temperature amplitude linked to the thermoelastic coupling measured by infrared camera
$\theta^s_{the_a}$	Temperature amplitude linked to the thermoelastic coupling
θ^s_{the}	Temperature linked to the thermoelastic coupling
θ	Temperature variation of a sample under mechanical loading
$\overline{R_z^{x,z}}$	Ten-point height roughness averaged on a surface for profiles perpendicular to the building direction and along the building direction, respectively
R_z	Ten-point height roughness
λ	Thermal conductivity
C_{the}	Thermoelastic coupling heat source
C_t	Threshold offset value of the image post-processing protocol
V_t	Threshold value of the image post-processing protocol
t_0	Time corresponding to the reference state (undamaged sample)
σ_{UTS}	Ultimate tensile stress
σ_y	Yield stress
E	Young modulus

1 Introduction

Metal Additive Manufacturing (AM) processes are of great interest to industrial figures as they enable the manufacturing of unprecedented complex designs (hollow bodies, optimized shapes, *etc*.) and tend to guarantee cost efficiency. Out of currently known AM techniques, Wire and Arc Additive Manufacturing (WAAM) is the best-suited to the production of large parts given its deposition rate of a few kilograms per hour.[1] WAAM is a direct energy deposition process: parts are built on a substrate by stacking layers of juxtaposed weld beads, using welding wire as material input. A typical WAAM building unit is composed of industrially sound equipment, such as a robotic arm and a welding torch, making this process highly modular and cost competitive. AM techniques constitute a real breakthrough in the industrial production process as only one step is required to progress from the numerical design of a part to its actual realization. Indeed, AM parts are said to be "near net shape", meaning they require little to no finishing operations. However, the surfaces of as-built AM geometries usually present significant roughness that can be extremely detrimental to the fatigue life.[2–4] This roughness is highly dependent on the AM technique under consideration. In the case of powder-based AM processes, such as Selective Laser Melting (SLM), the roughness is due to residual un-melted grains on the surface. An arithmetic average roughness R_a under 50 µm to only a few micrometers is typically measured.[5,6] In the case of Direct Energy Deposition (DED) AM techniques, such as WAAM, surface roughness is the result of the geometry's discretization in layers and weld beads; the roughness R_a can be more than a hundred microns.[7,8] In order to avoid a systematic and complete machining of AM parts, the effect of the as-built roughness on mechanical properties, especially in fatigue, must be carefully taken into account.

Extensive work has been published on the subject of as-built surfaces' effects on fatigue performances of AM parts, especially for the SLM process. The proposed fatigue approaches can be divided into two categories, namely crack propagation approaches and crack initiation approaches. The crack propagation methods are traditionally inspired by a Murakami type approach[9] in which a defect is considered as an initial crack. To characterize this initial crack in the case of AM rough surfaces, its size is usually assimilated to a selected roughness parameter. In the work of Wycisk et al.,[10] concerning a Ti-6Al-4V fabricated through SLM, the maximum height of the profile R_t (delta of altitude between the highest peak and the lowest value of a roughness profile) is chosen as the initial crack size. It is argued by Yadollahi et al.[2] that the value of R_t takes into account the presence of partially melted grains that are not cohesive with the surface, and so are not critical in regard to fatigue. Instead, the use of the maximum valley depth below the mean line R_v is suggested as the initial crack size. Then, multiple fatigue life curves are calculated based on the FASTRAN code[11] (calibrated from standard crack growth test results) and considering different values of R_v, as measured on various surface scans. A good level of coherence is found between experimental results and the model forecasts for the lower stress levels, but more pronounced differences are found under higher stress levels, suggesting that the nature of the critical defects would depend on the stress level.[12,13] In the work of Sanaei et al.[14] on powder-based AM techniques, both the effect of surface roughness and sub-surface defects are considered in a single indicator of crack size, derived from the definition of the effective area proposed by Masuo et al.,[15] whereby both the roughness R_t and the mean altitude range of the profile are considered. It is then proposed to determine the fatigue life either through Paris law or through a modified NASGRO.[16] In the field of crack initiation approaches, the work of Pegues et al.[3] on SLM also makes use of roughness parameters in order to define a fatigue knock-down ratio, as compared to fully machined AM specimens. A rather different approach is proposed by Vayssette et al.[17] concerning the SLM process: the Crossland fatigue criterion[18] is evaluated on digitized rough surfaces and averaged over a zone defined by a selected critical distance. This allows for the unification of machined and as-built samples fatigue results for the lower stress levels while differences at higher stresses are observed due to the criterion parameters determined at a 2×10^6-cycle life.

For the WAAM process, the rough surface state to be taken into consideration is relatively different to that in SLM. The development of approaches dedicated to the fatigue dimensioning of as-built WAAM parts is rather scarce in the literature available. In the work of Samadian et al.,[19] a crack propagation model is proposed in which the presence of stress concentrations at the surface is taken into account through a short crack - long crack type approach. No experimental data was considered to validate the proposed model. In the work of Bartsch et al.[7] a Basquin law is identified on experimental fatigue lives of rough WAAM samples. Based on numerical calculations performed on the digitized roughness profiles of the samples, a stress concentration factor K_t is determined and associated with the experimental fatigue lives. Then, randomly generated roughness profiles, supposedly representative of a real WAAM surface state, are used to define a relationship between fatigue properties and various roughness parameters based on the numerical K_t values.

This short literature review shows that, in the specific case of WAAM, because of an unprecedented roughness that is highly dependent on the deposit strategy, an empirical relationship between stress concentration K_t and surface state parameters is yet to be determined. From the study conducted by Bartsch et al.,[7] no obvious correlation appears to exist between K_t and some selected local geometry variables. To further explore that approach would require highly detailed 3D scans and costly numerical simulations. As for crack propagation approaches, there is a lack of experimental data which would allow us to determine the impact of the extremely rough WAAM surface on crack propagation kinetics in order to establish a dedicated fatigue model to assist manufacturers in determining the best deposit strategy regarding fatigue life of as-built WAAM structures.

In light of this, an experimental method is proposed in the present study to characterize fatigue cracks initiation and propagation in the case of rough as-built WAAM bronze-aluminum specimens. To achieve this, samples with a surface state representative of a real structure have been subjected to four-point bending constant amplitude cyclic loading and monitored with an infrared camera in order to perform Thermoelastic Stress Analysis (TSA). Indeed, this experimental method is especially suited to the characterization of surface fatigue cracks. Given suitable experimental precautions, TSA allows for the estimation of stress intensity factor ranges,[20–22] the characterization of the dissipation behaviour at the crack tip[23] and the crack propagation monitoring.[24,25] In the present paper, TSA is used in order to monitor cracks and describe their propagation kinetics: as the presence of surface cracks directly affects the observed field, the detection of their initiation and the monitoring of their propagation is made possible through image processing.

This paper is divided into four sections. Firstly, the WAAM material used for the study and its rough as-built surface are presented as well as the experimental set-up. Secondly the principle of the TSA methodology is explained, within the context of bending fatigue tests. Then, a protocol is proposed to allow for the detection of cracks, using the recorded infrared films. Further analysis shows that the crack initiation sites are correlated, to an extent, with highly stressed regions on the rough surface. Finally, an image post-processing technique is presented in order to allow for the monitoring of crack propagation. The generated data is shown to be of great interest for the identification of a dedicated crack propagation model.

2 Material and experimental set-up

In this section, the studied material, and its rough as-fabricated surface, is analyzed. Then, an experimental protocol is set to determine the corresponding properties in fatigue.

2.1 As-fabricated WAAM surface

The material used for this study is a $CuAl9Ni5Fe4$ (wt%) bronze-aluminum built by WAAM. It was produced by Naval Group and provided in the form of multi-bead heat-treated twin blocks of approximate dimensions 450 mm $\times$ 220 mm $\times$ 35 mm (Fig.1). The WAAM process deposition parameters are constant throughout the study and are representative of real industrial application. Those parameters are not disclosed herein. The values of the density ρ, α' the coefficient of thermal expansion, the specific heat capacity c and the thermal conductivity λ are given in Table 1. The mechanical properties of the machined WAAM bronze-aluminum material

E (GPa)	σ_y (MPa)	σ_{UTS} (MPa)	$A_{\%}$ (%)	ρ (kg.m^{-3})	α' (K^{-1})	c (J.kg^{-1}.K^{-1})	λ (W.m^{-1}.K^{-1})
113	394	852	19	6700	17×10^{-6}	460	35

TABLE 1 – Thermomechanical properties of the WAAM bronze-aluminum

were determined through quasi-static tensile tests using an MTS servo-hydraulic testing machine with a capacity of 250 kN. Tests were performed only in the building direction. Indeed, it is typically observed that, for such WAAM materials, there is little to no anisotropy at the macroscopic scale.[26–28] The Young modulus E, the yield stress σ_y, the ultimate tensile stress σ_{UTS} and the deformation to failure $A_{\%}$ are given in Table 1. For further details on the properties of the machined WAAM bronze-aluminum, refer to.[29]

The rough surface of samples extracted from the blocks was analyzed using a Keyence VHX 5000 optical microscope. 3D measurements were performed in order to estimate roughness parameters over areas of approximately 37 mm $\times$ 37 mm. The altitude map of one sample and roughness profiles (with an exaggerated scale in y) in the x and z directions are shown in Fig.1. The arithmetic average height R_a and the ten-point height R_z are calculated following

$$\begin{cases} R_a = \frac{1}{n}\sum_1^n |y_i|, \\ R_z = \frac{1}{5}\left(\sum_1^5 p_i - \sum_1^5 v_i\right) \end{cases} \tag{1}$$

with y_i the signed distance to the mean altitude, p_i the altitude of one of the five highest peaks and v_i the altitude of one of the five deepest valleys. These roughness parameters are calculated along two directions : perpendicular to the building direction (x, along the layers) and along the building direction z ; their mean value over one sample surface are gathered in Table 2. From this measurement, it can be observed that the surface roughness is anisotropic : a more pronounced roughness is found along the building direction z, due to the geometry discretization in layers, which are approximately 3 mm in thickness. In this study, a mechnical loading of maximum principal stress along the building direction z is considered ; the effect of the anisotropic roughness is not taken into account. In Fig.1, a welding projection can be found at $(x; z) = (22.5; 28)$. While such asperity appears in the altitude map and can affect the calculation

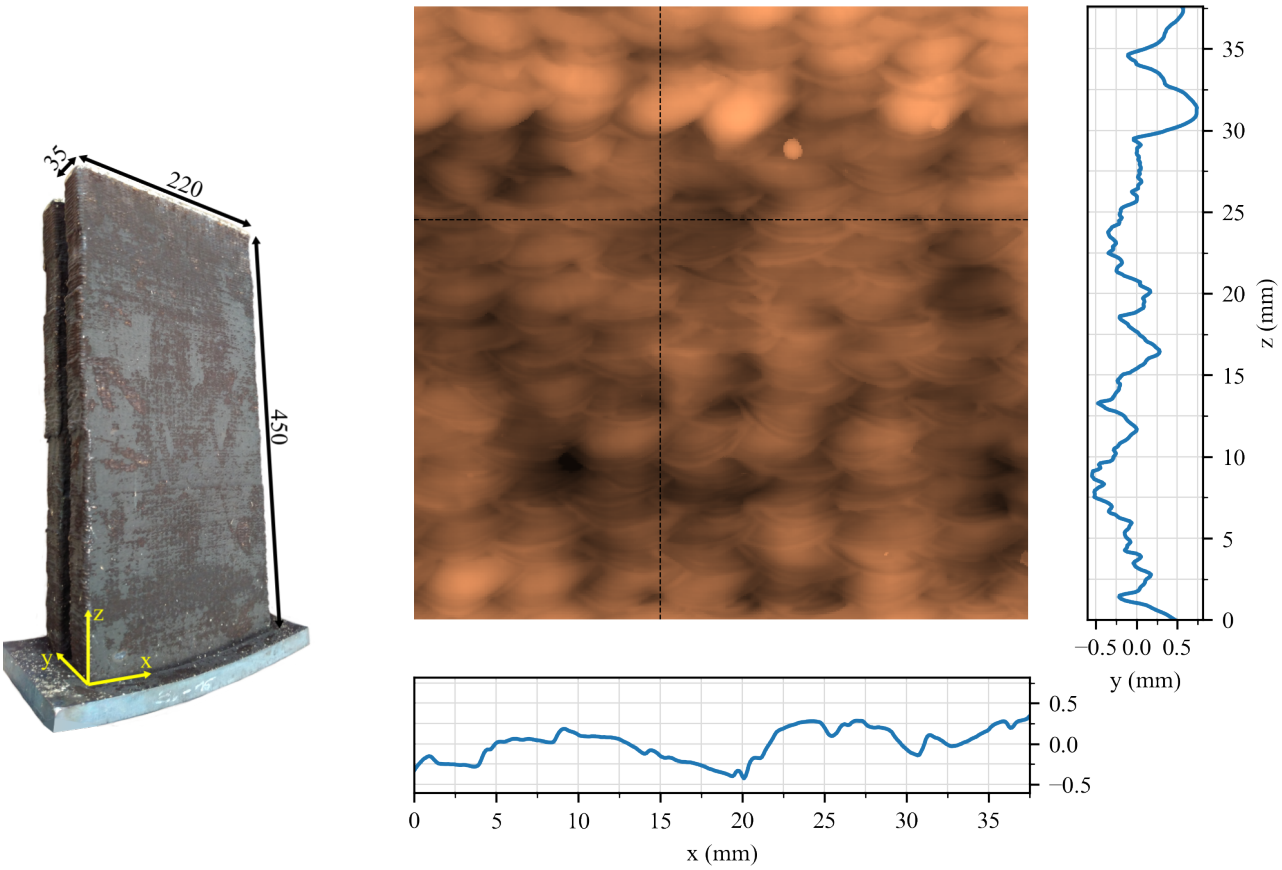

(a) (b)

FIGURE 1 – Twin blocks of WAAM bronze-aluminum for the study on the rough surface effect on fatigue properties (all dimensions in millimeters) (a) and altitude map as measured with a Keyence VHX 5000 optical microscope and selected roughness profiles along directions x and z (altitude y scale is exaggerated) (b)

of a numerical stress field, it is not a critical site in terms of fatigue as welding projections are not cohesive with the surface.

$\overline{R_a^x}$ (µm)	$\overline{R_a^z}$ (µm)	$\overline{R_z^x}$ (µm)	$\overline{R_z^z}$ (µm)
171	236	515	565

TABLE 2 – Roughness parameters' mean values over a sample surface in both directions x and z

2.2 Test specimen

Parallelepipedal test specimens of dimensions 180 mm × 40 mm × 15 mm* were extracted from the rough WAAM blocks by wire electrical discharge machining (Fig.2a). One face of the sample is left as-built while the other one is machined. Small areas are machined at both ends of the rough face to allow for the specimen setup in the testing machine. All specimens are edged to prevent crack initiation due to geometric singularities which are unrepresentative of the rough surface.

Given the significant roughness of the samples' as-built surface, a convention must be set to define a nominal stress. In this study, it was selected to consider the stress in a flat median shell which thickness t_{nom} (Fig.2b) is defined as

$$t_{nom} = t_{build} - \frac{R_z}{2} \approx t_{build} - R_a \approx 14.75\, mm, \tag{2}$$

with t_{build} the thickness of the minimum containing parallelepipedal shell, equal to 15 millimeters. It is important to keep this conven-

∗. In practice the 15 mm thickness is selected equal to the height of the parallelepiped with its rough face against a flat surface.

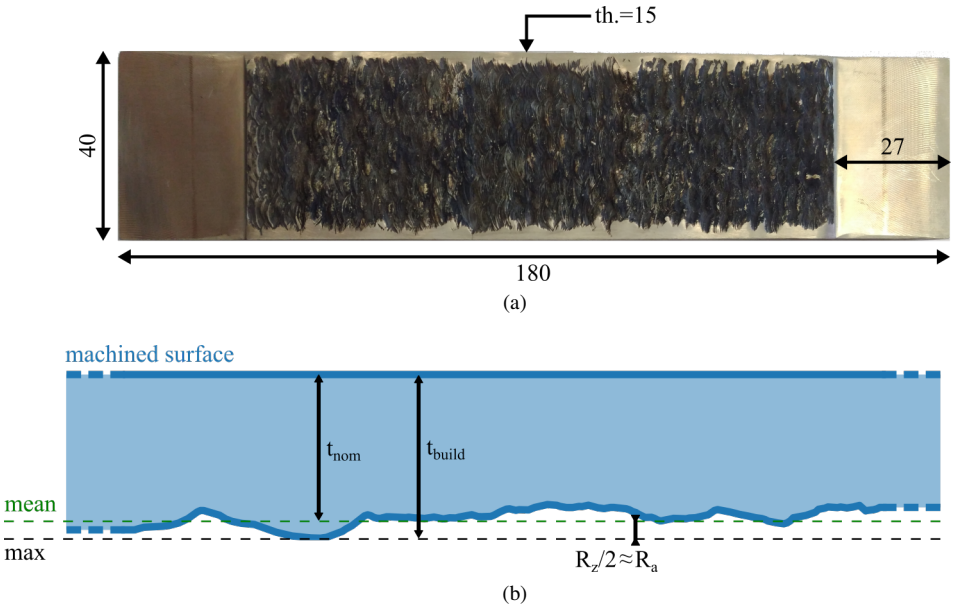

FIGURE 2 – Test specimen dimensions in millimeters (a) and definition of the nominal thickness t_{nom} (b)

tion in mind as the stress levels considered in a SN curve depend on it. Indeed, the WAAM roughness is such that the choice of a nominal thickness can significantly affect the knock-down ratio when compared to the fatigue properties of fully machined samples.

2.3 Experimental protocol

In order to promote the initiation of fatigue cracks on the rough surface, the samples are subjected to four-point bending cyclic tests. Tests are performed at a loading ratio $R = \frac{F_{min}}{F_{max}}$ (with F_{min} and F_{max} the minimum and maximum load, respectively) of 0.1 and a mechanical frequency f_m of 5 Hz using a force-controlled MTS servo-hydraulic testing machine with a capacity of 250kN. Tests are carried out until fatigue failure of the sample, corresponding to an increase of 50% in displacement magnitude of the actuator.

The samples are coated with high-emissivity black paint. Given the orientation of the sample in the four-point bending test fixture, an infrared mirror (of a 98% reflectivity) tilted at $45°$ is used to monitor the temperature field on the rough surface via an infrared camera FLIR SC7600 (Fig.3). Infrared films of a 512×640-pixel resolution and a 100 Hz sampling frequency are recorded during 150 loading cycles at a regular time interval. It must be noted that despite the significant roughness of the observed surface, the altitude variations are relatively smooth and there are very few points where the surface normal angle exceeds $60°$ with the camera direction. According to the study by Vollmer and Möllmann[30] on the effect of the observed surface normal on the emissivity, this surface condition appears to be compatible with an infrared thermography instrumentation †. Indeed, the angle of the surface normal to the camera direction is estimated atunder $60°$ for digitized samples. The spatial resolution of the infrared film on the surface of the rough samples is 260 µm for one pixel.

In this study, the experimental results of 6 samples, labelled from SPI to $SPVI$, are considered. The nominal stress amplitude $\sigma_{a_{nom}}$ is defined as the bending stress amplitude at the skin of a flat sample of thickness t_{nom}

$$\sigma_{a_{nom}} = \frac{3}{4}\left(\frac{(F_{max} - F_{min})(L - l)}{w{t_{nom}}^2}\right), \tag{3}$$

with L the distance between the two support points, l the distance between the two load application points and w the width of the sample. The value of the nominal stress amplitude $\sigma_{a_{nom}}$ applied for each sample is given in Table 3.

Sample	SPI	$SPII$	$SPIII$	$SPIV$	SPV	$SPVI$
$\boldsymbol{\sigma_{a_{nom}}}$ **(MPa)**	94	75	70	62	78	70

TABLE 3 – Nominal stress amplitude values of the tested samples

†. At least without any emissivity correction due to geometrical effects.

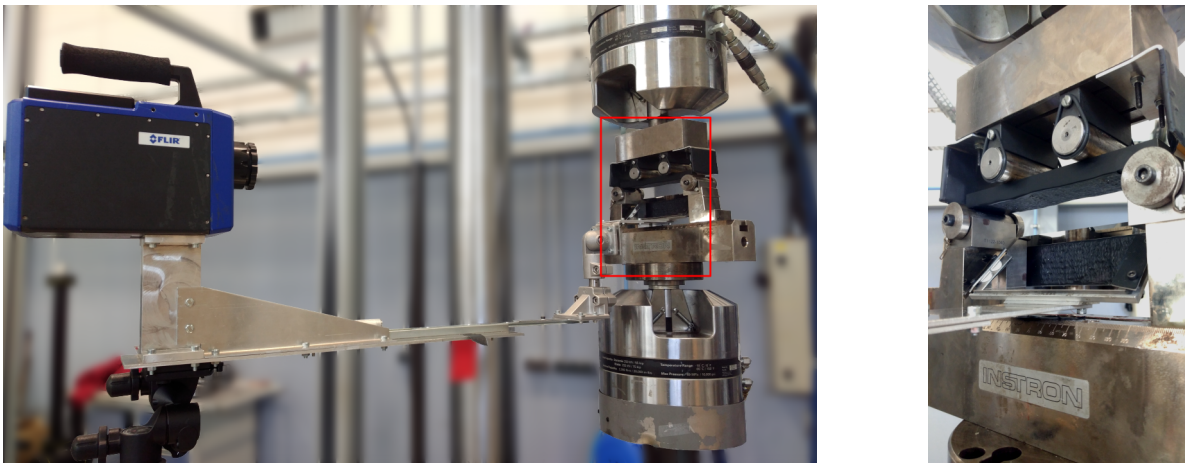

(a) (b)

FIGURE 3 – Image of the four-point bending test fixture and the infrared camera (a) and zoom showing the mounted sample and the infrared mirror (b)

3 Thermoelastic Stress Analysis (TSA)

Thermoelastic Stress Analysis is an experimental method with an aim of providing in-situ monitoring of the stress field on a surface from infrared data. In this section, a short background theory is given on TSA. Then, an infrared data processing method based on the lock-in method,[31–33] used to compute the temperature amplitude linked to the thermoelastic coupling, is presented.

3.1 Thermoelastic coupling

The temperature response of a sample subjected to cyclic mechanical loading can be decomposed in two parts (Fig.4)

— the intrinsic dissipation, leading to the progressive temperature rise of the sample which stabilizes at the value θ_d over a few cycles (assuming a constant mean heat source per loading cycle) ;

— the thermoelastic coupling, which corresponds to the immediate thermal response of the material to a mechanical loading: for a linear problem, a cyclic mechanical loading generates a cyclic thermal response of amplitude $\theta^s_{the_a}$.[34]

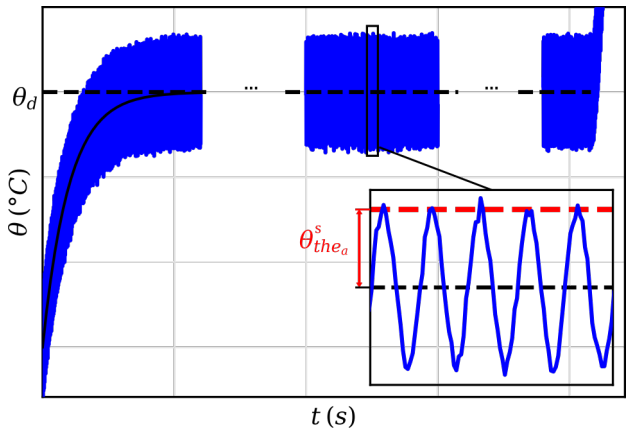

FIGURE 4 – Schematic illustration of the sample's surface mean temperature variation θ during a complete fatigue test, composed of an intrinsic dissipation contribution θ_d and a thermoelastic contribution $\theta^s_{the_a}$

In this study, the analysis of the thermoelastic contribution to the temperature signal is of particular interest, as it gives information on the stress field of the observed surface. Indeed, from the local heat equation comes

$$\rho c \frac{\partial \theta}{\partial t} = -div\,(\overrightarrow{q}) + C_{the} + \Delta, \tag{4}$$

with θ the temperature variation, $\overrightarrow{q}$ the vector of local heat flux and C_{the} and Δ the heat sources of thermoelastic coupling and dissipation, respectively. Considering small temperature variations (*i.e.* $\frac{\theta}{T_0} \ll 1$ with T_0 the initial temperature), given that the present material is isotropic, verifies ${\alpha'}^2 \frac{3E}{1-2\nu} T_0 \ll \rho c$ and is working in its elastic domain, the heat source C_{the} of the thermoelastic coupling is expressed as

$$C_{the} = -\alpha' T_0 \frac{\partial I_1}{\partial t}, \tag{5}$$

with I_1 the stress tensor's first invariant. In the case of a sinusoidal loading in the elastic domain of the material, it comes[35]

$$C_{the} = 2\pi f_m \alpha' T_0 I_{1_a} sin\left(2\pi f_m t - \frac{\pi}{2}\right), \tag{6}$$

with f_m the mechanical loading frequency and I_{1_a} the amplitude of the stress tensor's first invariant. By solving the local heat equation (Equation 4), assuming adiabatic conditions within one cycle (negligible conduction), the immediate temperature response linked to the thermoelastic coupling θ^s_{the} is expressed

$$\theta^s_{the}(t) = I_{1_a} \frac{\alpha' T_0}{\rho c} cos\left(2\pi f_m t + \frac{\pi}{2}\right), \tag{7}$$

with ρ the density and c the specific heat capacity. The temperature amplitude linked to the thermoelastic coupling $\theta^s_{the_a}$ is

$$\theta^s_{the_a} = I_{1_a} \frac{\alpha' T_0}{\rho c}. \tag{8}$$

The temperature amplitude $\theta^s_{the_a}$ is proportional to the amplitude of the stress tensor's first invariant. In that sense, the field of the temperature amplitude $\theta^c_{the_a}$ over a surface observed by an infrared camera gives an information on the stress tensor's first invariant amplitude field.

In practice, given the experimental set-up and the loading frequency $f_m = 5Hz$, conduction effects are not negligible, meaning that adiabatic conditions are not reached. As a result, the field of temperature amplitude $\theta^c_{the_a}$ linked to the thermoelastic coupling computed from the experimental infrared data is not a direct image of the first invariant's amplitude I_{1_a} local field, but rather an image of a locally averaged I_{1_a} field. The extent of this conduction effect can be estimated through the evaluation of the characteristic length d_c in the expression of the Fourier number $\mathscr{F}$

$$\mathscr{F} = \frac{4\lambda}{\rho C f_m d_c^2}. \tag{9}$$

Depending on the material and the test condition (*i.e.*, mechanical frequency f_m), three cases must be considered:

— $\mathscr{F} << 1$: conduction is negligible (*i.e.*, adiabatic condition);

— $\mathscr{F} = 1$: heating capacity and conduction are of the same order of magnitude;

— $\mathscr{F} >> 1$: conduction is preponderant.

By imposing $\mathscr{F} = 1$, the characteristic length $d_c = 3$ mm is found, meaning that heterogeneities in the field of temperature amplitude $\theta^c_{the_a}$ of size smaller than 3 mm cannot be observed. This precision is compatible with the observation of WAAM rough surfaces as the layer thickness measures approximately 3 mm: the stress heterogeneities induced by the layers can be observed through thermoelastic stress analysis (as seen in Fig.5b).

3.2 The lock-in method

In order to compute the maps of temperature amplitude $\theta^c_{the_a}$ linked to the thermoelastic coupling, the lock-in method[31] was implemented in the homemade software Celenos[36] which is dedicated to infrared data post-processing. This signal post-processing techniques is a useful and efficient tool for the detection of specific mechanical events from infrared data such as the initiation and propagation of cracks.[32,33] This method consists in multiplying a measured signal F by a correlation function K

$$S = \frac{1}{nN_P} \sum_{i=1}^{N_P} \sum_{j=1}^{n} K_j F_{j,i}, \tag{10}$$

with N_P the number of periods contained in F (determined by the loading frequency f_m and the length of the infrared film) and n the number of data points contained in a period (determined by the sampling frequency f_s and the loading frequency f_m). The term

K is decomposed in two orthogonal components which expression is selected to match the sinusoidal mechanical loading

$$\begin{cases} K_j^0 = 2sin\left(2\pi\frac{j-1}{n}\right), \\ K_j^{-90} = -2cos\left(2\pi\frac{j-1}{n}\right). \end{cases} \tag{11}$$

The term K_j^{-90} allows for the consideration of a phase-shift effect between the mechanical loading and the temperature signal, caused by conduction effects. From these two components, it comes

$$\begin{cases} S^0 = \frac{1}{nN_P}\sum_{i=1}^{N_P}\sum_{j=1}^{n} K_j^0 F_{i,j}, \\ S^{-90} = \frac{1}{nN_P}\sum_{i=1}^{N_P}\sum_{j=1}^{n} K_j^{-90} F_{i,j}. \end{cases} \tag{12}$$

Then the amplitude A_l of the input signal F is

$$A_l = \sqrt{\left(S^0\right)^2 + \left(S^{-90}\right)^2} \tag{13}$$

and its phase Φ_l

$$\Phi_l = arctan\left(-\frac{S^{-90}}{S^0}\right). \tag{14}$$

In the context of the additive manufactured four-point bending test samples, the input signal F is the temperature signal of a pixel in the infrared film, and A_l is the temperature amplitude $\theta^c_{the_a}$ linked to the thermoelastic coupling in a pixel.

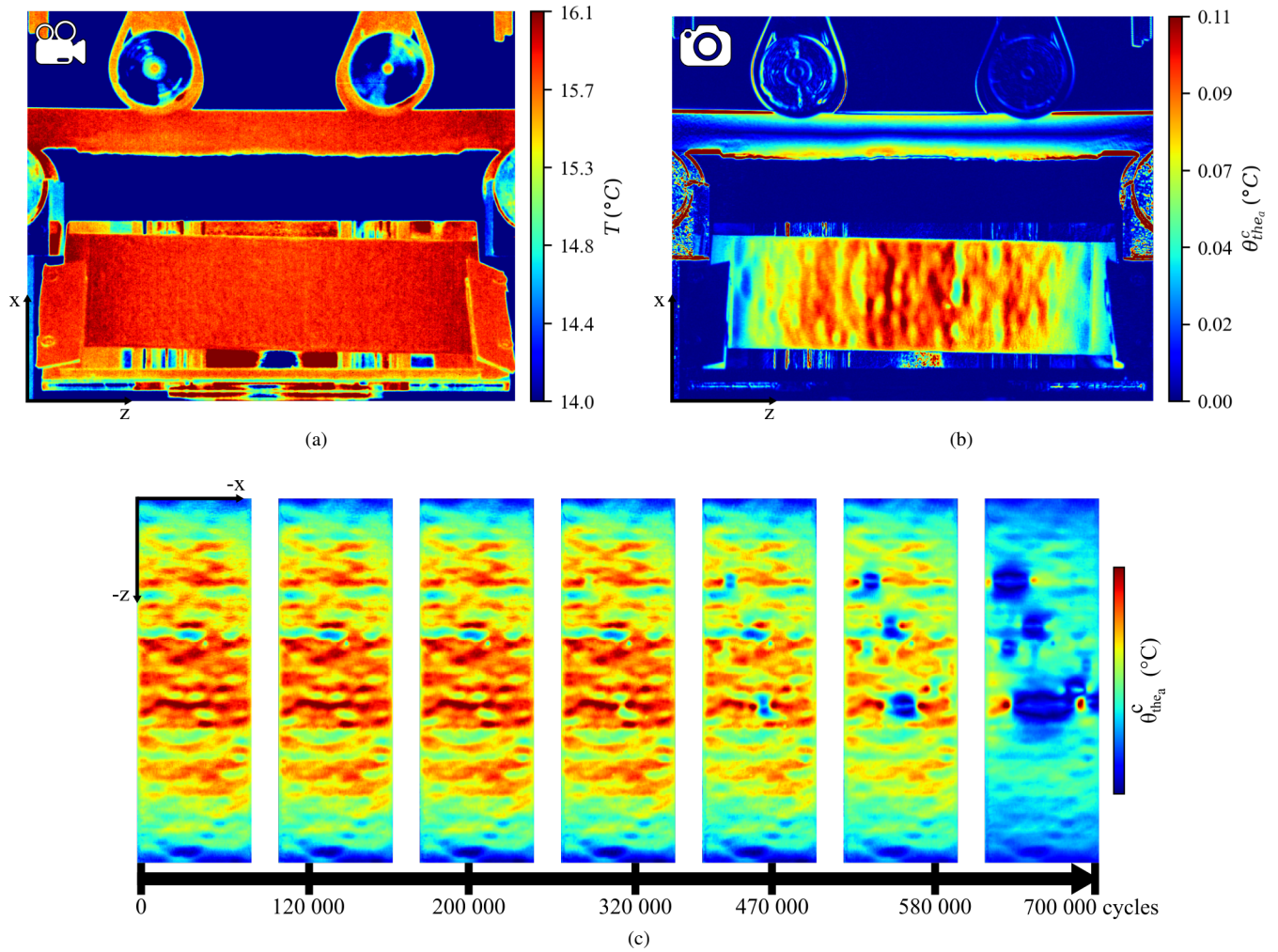

FIGURE 5 – Frame of an infrared film of $SPII$ (a), field of the temperature amplitude $\theta^c_{the_a}$ linked to the thermoelastic coupling of the corresponding infrared film as determined by the lock-in method (b) and evolution of the temperature amplitude $\theta^c_{the_a}$ field on the rough surface of sample $SPII$ during its fatigue test (c)

For each film (Fig.5a) that is recorded during a fatigue test, the lock-in method is applied to every pixel in order to compute the field of the temperature amplitude $\theta^c_{the_a}$ linked to the thermoelastic coupling (Fig.5b), image of a locally averaged I_{1_a} field at a given number of cycles. The camera field of view allows for the observation of both the rough surface of the sample as reflected by the infrared mirror (at the bottom of the images in Fig.5) and the side of the sample (at the top of the images in Fig.5). On the temperature amplitude $\theta^c_{the_a}$ field (Fig.5b), the stress concentrations on the rough surface caused by the layer discretization can be seen, which is coherent with the determined value of the characteristic length $d_c = 3\ mm$. On the side of the sample, a typical bending stress field can be observed.

By looking at the evolution of the temperature amplitude $\theta^c_{the_a}$ field of the as-built surface during the fatigue test (Fig.5), it is possible to witness the initiation of cracks, that appear as perturbations in the initial $\theta^c_{the_a}$ field, and their propagation until the fatigue failure of the sample.

4 Crack detection

By analyzing the evolution of the temperature amplitude $\theta^c_{the_a}$ field on the samples rough surface during a fatigue test, it is possible to detect the presence of surface cracks. This is achieved through the use of image processing techniques, which are detailed in the following paragraph.

4.1 Detection method

The presence of cracks in an image of the temperature amplitude $\theta^c_{the_a}$ field is achieved through two steps:

— firstly, the reference image of the field of $\theta^c_{the_a}$ at $t = t_0$, prior to initiation of fatigue cracks, is subtracted to the current image ;

— then, a thresholding method is applied to the differential image, in order to create a binary image whereby the field affected by the presence of a crack is indicated by a value of 1 while the initial crack-free field is indicated by a value of 0.

4.1.1 Differential measurement

In the case of the rough surface samples fabricated by WAAM, the initial stress field (when no fatigue cracks have initiated yet) is heterogeneous, making it difficult to detect with precision small field heterogeneities when a surface crack appears. In order to get rid of this initial field heterogeneity, images of the differential of temperature amplitude $\Delta\theta^c_{the_a}$ are computed following

$$\Delta\theta^c_{the_a}(x,z,t) = \theta^c_{the_a}(x,z,t) - \theta^c_{the_a}(x,z,t=t_0)\,, \tag{15}$$

whereby x and z are the $2D$ coordinates of a mechanical point on the rough surface, t is the time and t_0 corresponds to the time of recording for the first infrared film, at the beginning of the fatigue test, prior to any fatigue damage. To allow for this linear operation between the same field at two different times, it must be ensured that x and z are time independent, meaning that any rigid body movement must be compensated between t_0 and t. In practice, rigid body correction is made possible by drawing markers on the rough surface with a metallic paint, which has low emissivity making the markers visible on the infrared data. The field of the differential of temperature amplitude $\Delta\theta^c_{the_a}$ is then exempt from the initial stress heterogeneities due to the rough as-built surface asperities. This image subtraction step is very important as it allows for an easy detection of thermal events (such as crack initiation) despite a strongly heterogeneous initial temperature field. This subtraction operation is performed for every image of the temperature amplitude $\theta^c_{the_a}$ field, computed from each infrared film. The evolution of the field $\Delta\theta^c_{the_a}$ on the rough surface of sample $SPII$ is illustrated in Fig.6a. It can be observed that the first two images, at the beginning of the fatigue test, appear to be homogeneous and plain, as no cracks have yet been detected. Then, at $200\,000$ cycles, a thermal event can be observed in the center of the sample, where a blue dot appears, meaning that stress has dropped locally. In the following images, for a higher number of cycles, these thermal events multiply and grow until they reach the width of the sample. These thermal events correspond to the initiation and propagation of fatigue cracks. Indeed, near a crack, the stress tensor's first invariant I_{1_a} field is easily recognizable: there are stress concentrations at the crack tips and zero stress at the free edges (Fig.6b). As the temperature amplitude $\theta^c_{the_a}$ is linked to I_{1_a}, near the crack edges $\theta^c_{the_a}$ drops and $\Delta\theta^c_{the_a}$ is negative (blue stain on Fig.6c) ; at the crack tips $\theta^c_{the_a}$ rises and $\Delta\theta^c_{the_a}$ is positive (red spots on Fig.6c).

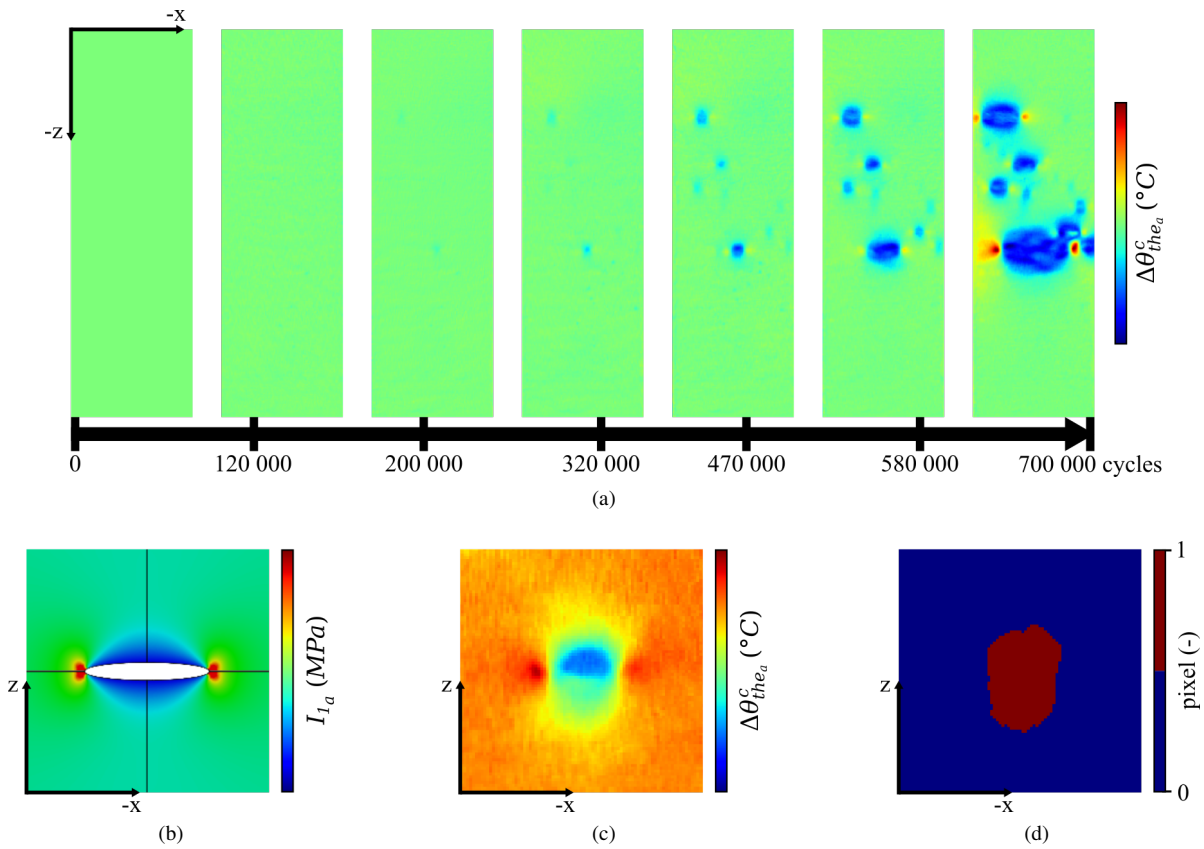

FIGURE 6 – Evolution of the differential of temperature amplitude $\Delta\theta^c_{the_a}$ field on the rough surface of sample $SPII$ during its fatigue test (a), illustration of the I_{1_a} field around a fictive 2D crack in mode I (b), experimental $\Delta\theta^c_{the_a}$ field around a crack in a rough WAAM surface (c) and corresponding binary image after thresholding (d)

4.1.2 Image thresholding

In order to automate the process of crack detection, images are binarized, retaining only the information of the position and the size of cracks. This is done by thresholding the images: pixels which value are below a selected threshold are assigned to 1, while pixels above the threshold are assigned to 0. The goal is to distinguish the crack's affected field of $\Delta\theta^c_{the_a}$ (where the stress is relaxed at the free edges of the crack) from the image background (where $\Delta\theta^c_{the_a}$ is close to zero, meaning that $\theta^c_{the_a}$ is unchanged from the initial state at t_0). This is shown in Fig.6d, where the red area represents the crack affected $\Delta\theta^c_{the_a}$ region, which extent depends on the chosen threshold value, and the blue area represents the unchanged initial field plus the crack tips.

As the region of interest (the sample's rough surface) is relatively large, the smaller cracks have no weight in the total image histogram. Then the choice of a single and constant threshold for all the infrared images generated for one fatigue test is not suitable. Rather a local thresholding technique is adopted, where a different threshold value V_t is selected for each pixel, equal to the Gaussian weighted average of the neighboring pixels minus an offset value. There are two adjustable parameters to this local thresholding: the size Z_t of the block around the analyzed pixel defining its neighborhood and the offset value C_t. These parameters must be chosen in order to detect smaller cracks without altering the shape of bigger cracks. In this study, values of $Z_t = 71 (\approx 19$ mm) and $C_t = 5$ were found to give satisfactory results. As this method is especially sensitive to experimental noise, the resulting binary images must be cleaned. In practice, successive steps of erosion, dilation and deletion of small elements are applied to the computed binary images. This binarization method is applied to every $\Delta\theta^c_{the_a}$ map (Fig.7). For each detected crack, the initiation site is assimilated to the centroid of the binarized area of the affected $\Delta\theta^c_{the_a}$ field at its first detection. This is illustrated in Fig.7 where white dots on the binarized image indicate the initiation site of each detected crack shown in red.

The minimal detectable crack total length following this protocol is found between 2 and 3 millimeters.

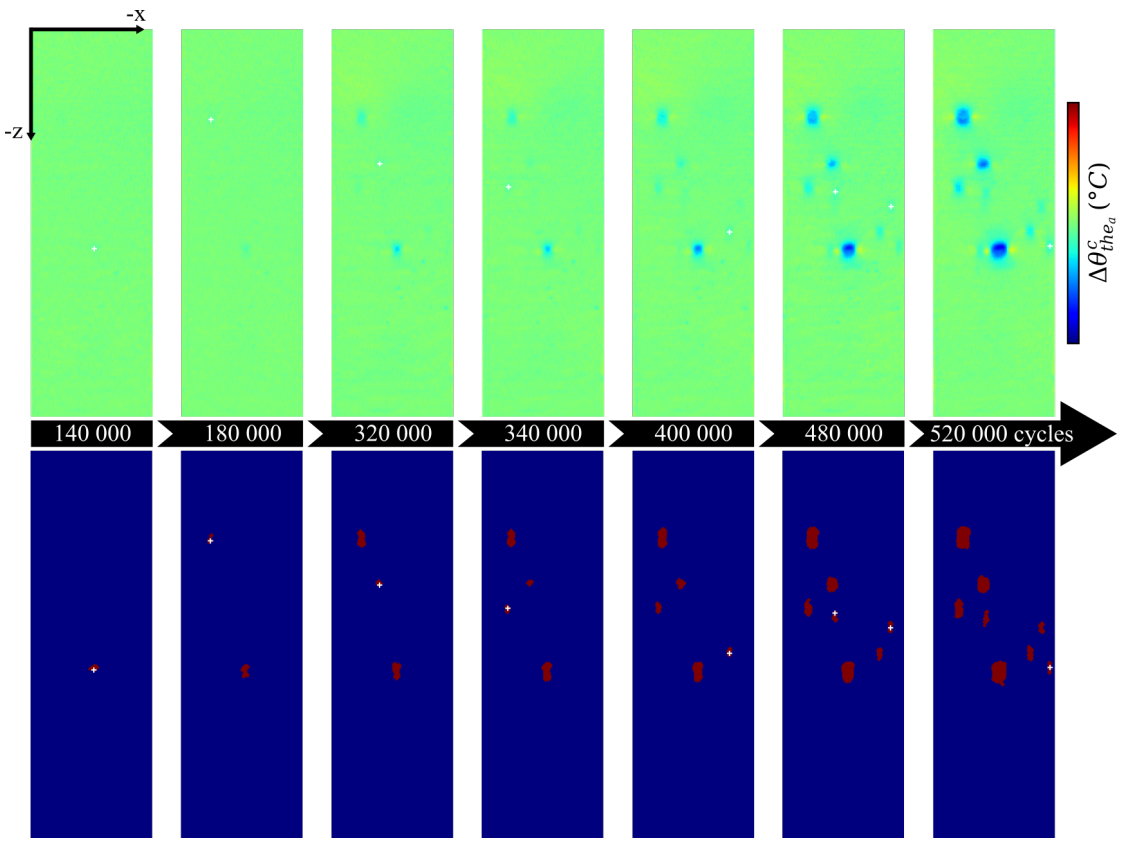

FIGURE 7 – Evolution of the differential of temperature amplitude $\Delta\theta^c_{the_a}$ field on the rough surface of sample $SPII$ with the corresponding binary images (initiation sites shown in white)

4.2 Crack initiation

While the exact local field of the stress tensor's first invariant amplitude I_{1_a} cannot be observed experimentally because of conduction effects, it can be estimated through numerical calculation using the mesh of a 3D scan of the rough surface. This allows for the correlation of crack initiation site and stress concentration factor K_{t_I} in the sense of the maximum principal stress amplitude σ_{a_I}, defined as

$$K_{t_I} = \frac{\sigma_{a_I}}{\sigma_{a_nom}}. \tag{16}$$

In Fig.8 is shown the superposition of the crack initiation sites, determined experimentally using the infrared data, over the numerically computed stress concentration factor K_{t_I} field. This comparison shows that, while every detected crack initiation site appears close to a high value of K_{t_I} (> 2), not every high K_{t_I} correspond to a crack initiation ; the correlation between K_{t_I} and crack initiation is not deterministic. An extensive experimental database could help in determining a probabilistic relation between crack initiation and K_{t_I} value or some parameters of the local geometry. However, it should be noted that the value of K_{t_I} at particularly severe surface asperities is difficult to determine with precision and needs costly computational efforts. Rather it is suggested to study the effect of WAAM process parameters such as layer height and bead width on the crack density and spatial distribution at constant stress amplitude using the proposed experimental protocol. Indeed, the field of K_{t_I} is strongly dependent on the surface geometry, which is controlled by the WAAM process.

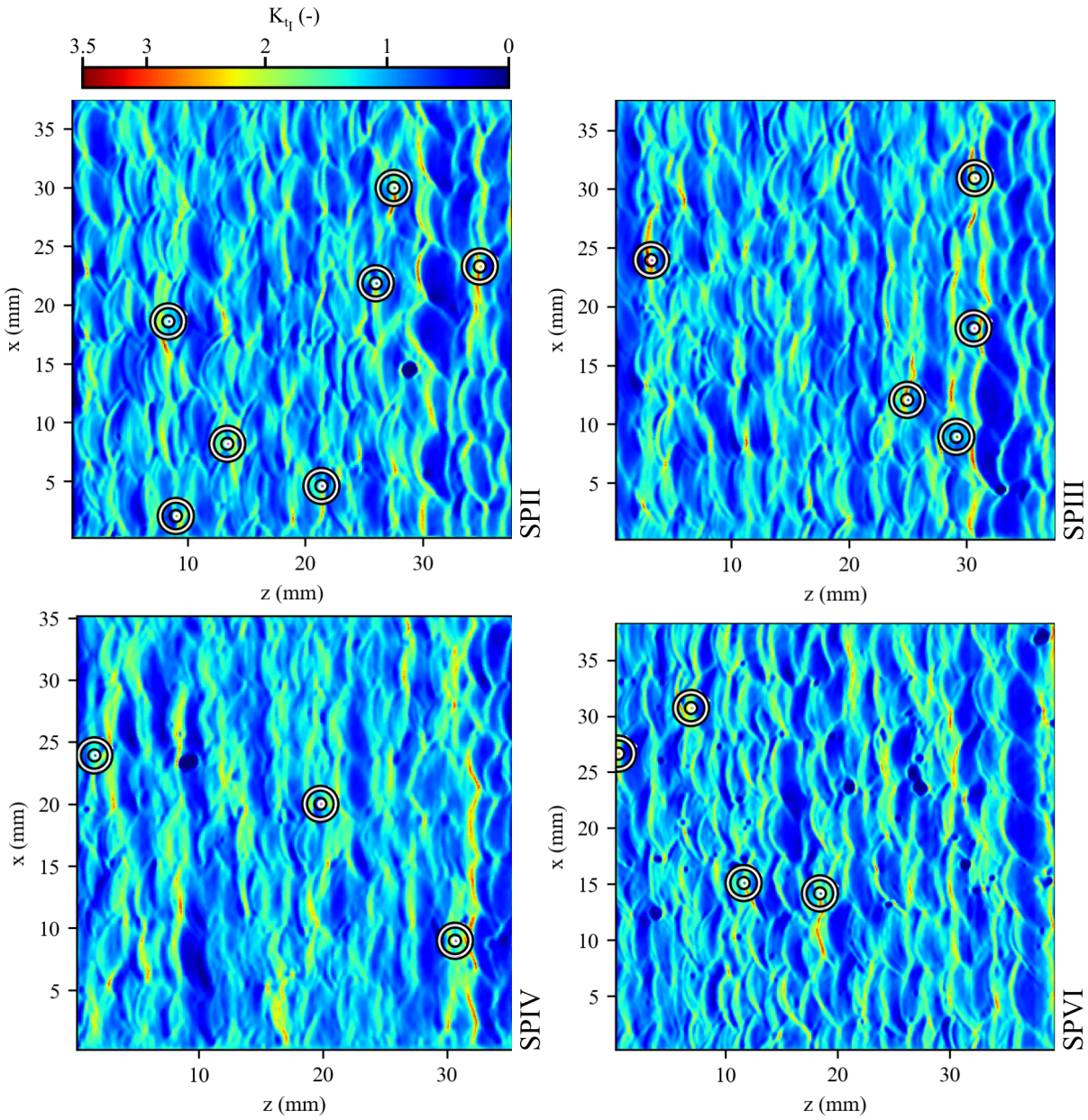

FIGURE 8 – Experimental crack initiation sites (in white) superposed over the numerical field of the stress concentration factor K_{t_I} for samples $SPII$, $SPIII$, $SPIV$ and $SPVI$

4.3 Crack interaction phenomena

A systematic multi-crack initiation phenomenon was observed for all tested samples. Given the rough surface and the density of surface irregularities, the existence of two crack interaction phenomena was revealed experimentally: the obscuration (or shielding) of cracks and coalescence.

Obscuration is the interruption of crack propagation due to a low stress field induced by the presence of a nearby larger crack. This is illustrated in the case of sample $SPIII$ in Fig.9a, where three cracks are detected: two are stopped in their propagation by the presence of the third larger crack, which is the only one to propagate until the end of the fatigue test. In practice, the obscuration of cracks makes it difficult to be detected through automatic binarization as the stress affected field of the cracks involved in the obscuration appear as a single binary zone.

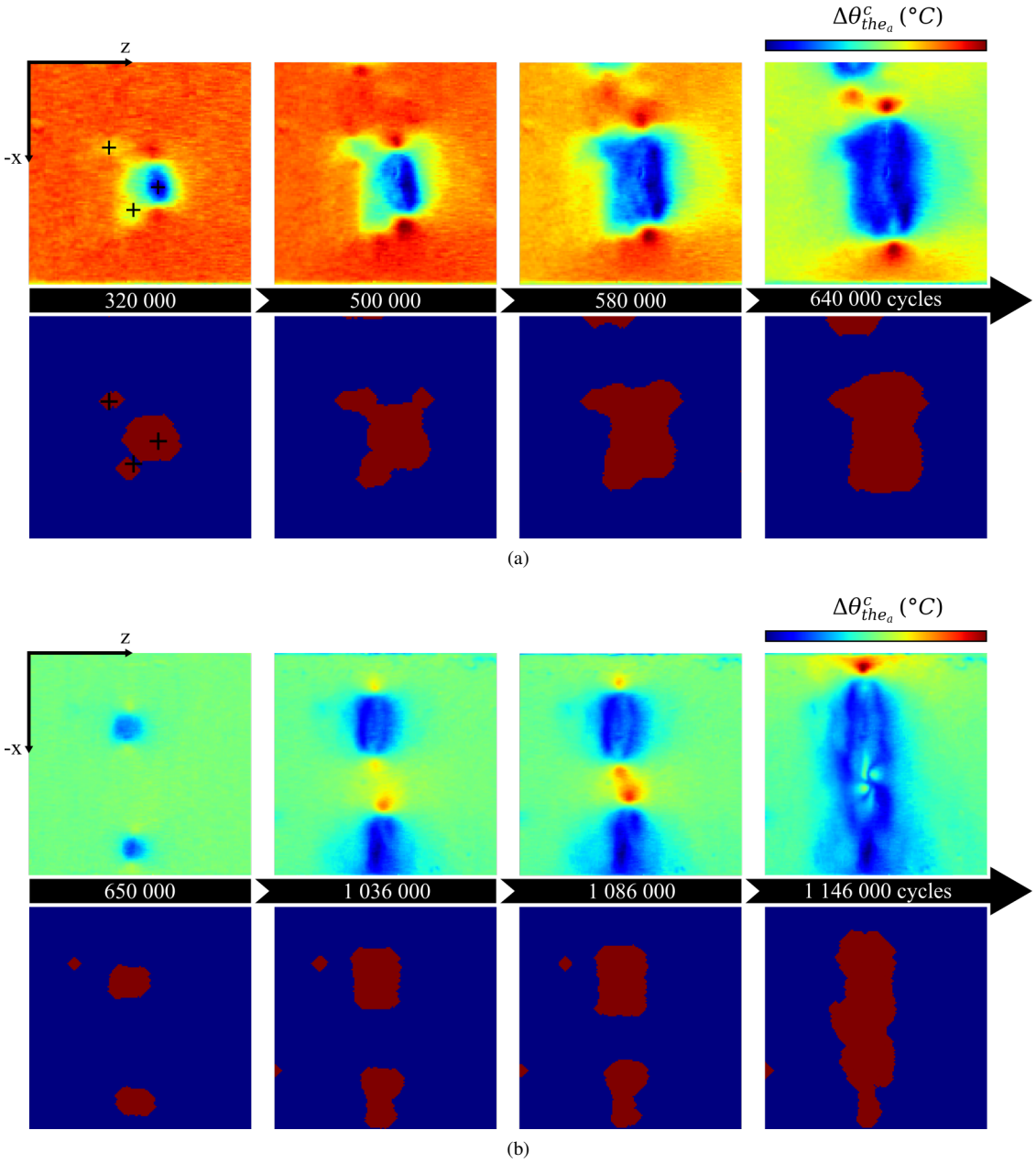

FIGURE 9 – Crack obscuration phenomenon demonstrated on sample $SPIII$: of the three cracks visible on the images, only one propagates throughout the whole fatigue life, as the two smaller cracks are obscured (a); and coalescence phenomenon on sample $SPIV$: two cracks initiate at a close z coordinate and propagate towards each other until meeting and merging (b)

Coalescence is the merging of two cracks during their propagation. In the case of WAAM rough surfaces in tension in the building direction, this happens when two cracks initiate between the same two layers or at close z coordinate. Indeed, the valley between two building layers is a stress concentration zone (Fig.8) where cracks can initiate and propagate, and so it is particularly prone to crack coalescence. This phenomenon is illustrated in Fig.9b for the case of sample $SPIV$.

4.4 Number of cycles to crack initiation

The proposed crack detection method allows for the definition of a number of cycles to crack detection N_d, which is the number of cycles at the detection of the first crack on the rough surface of a sample. Care is taken not to take into account the detection of non-significant events related to experimental noise or poor thresholding. This number of cycles required for crack detection N_d is compared to the total life N_r of the samples though the ratio N_d/N_r in Fig.10. It appears that at most 35% of the fatigue life consists of fatigue crack initiation, meaning that the fatigue life of the rough WAAM samples is dominated by a crack propagation mechanism. From this observation, a post-processing protocol for the tracking of crack propagation is put forward.

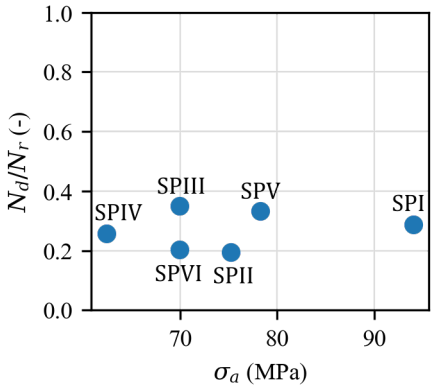

FIGURE 10 – Ratio of the number of cycles to crack detection N_d over the total fatigue life N_r for samples SPI to $SPVI$

5 Crack monitoring

Given the dominance of the crack propagation phase over the total fatigue life of rough WAAM samples (Fig.10), a post-processing protocol for the tracking of crack propagation is proposed in the following paragraphs.

5.1 Monitoring method

The binarization method used for the detection of cracks allows to determine the shape of the crack affected stress field. In order to determine with precision the size of the corresponding cracks and to characterize their propagation kinetics, the detection of the crack tips has been automated through the following steps, as illustrated in Fig.11a:

- a region of interest is delimited, centered around the binarized crack, and extended in the x direction ;
- a k-mean clustering algorithm is applied on this zone, in order to distinguish three domains according to the pixel values:
  - Domain I, corresponding to the crack center, where the stress is near zero and $\Delta\theta^c_{the_a}$ is the lowest ;
  - Domain II, corresponding to a transition zone around the crack ;
  - Domain III, corresponding to the crack tips, where the stress, and so $\Delta\theta^c_{the_a}$, is the highest ;
- a crack tip is then defined as a point at the intersection of Domain II and Domain III, aligned on the z coordinates of the maximum value in Domain III.

This post-processing method allows for the tracking of crack tips during the fatigue life of the rough WAAM samples. The crack path trajectory of sample $SPII$ is shown in Fig.11b. The post-processing method can be validated for the most critical cracks (that are still open and visible at the end of the fatigue test) by comparing the detected crack trajectory and the real crack trajectory determined by post-mortem optical microscope observations. Such comparisons were made for samples SPI to $SPVI$ (Fig.11c). Despite a few erroneous crack tip positions and the case of sample $SPVI$ where a crack near the edge is noted, the crack tip tracking method appears to be satisfactory.

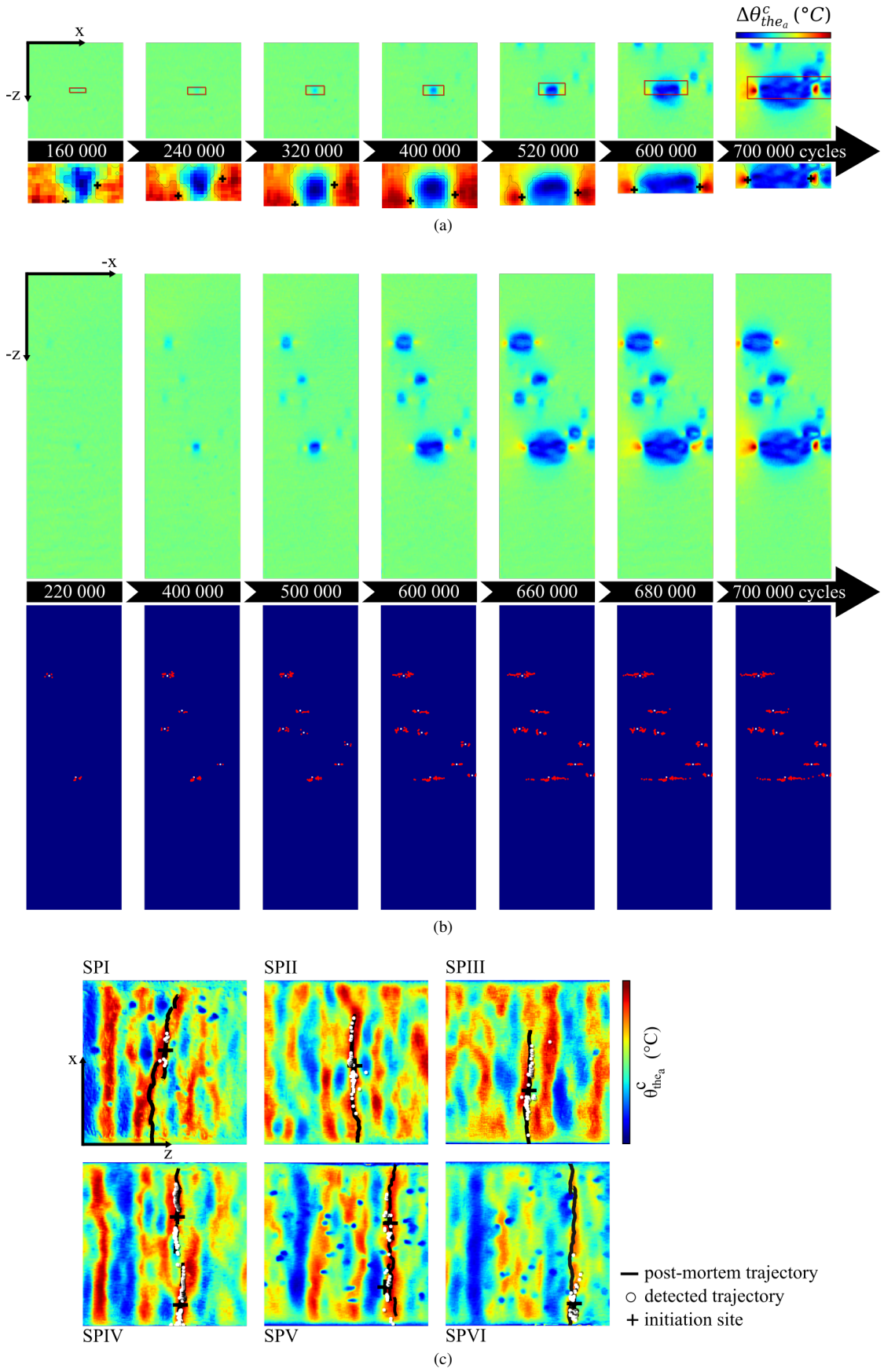

FIGURE 11 – Illustration of the crack tip detection method on an experimental WAAM rough surface crack: the $\Delta\theta^c_{the_a}$ maps over the black axis show the position of region of interest in red, while the images below show the detected position of the crack tips inside the region of interest (a), confrontation of the $\Delta\theta^c_{the_a}$ maps and the detected cracks tips trajectory throughout the fatigue life of sample $SPII$ (b) and comparison between the crack trajectories determined from the infrared films and the real crack trajectories determined from optical microscope post-mortem observations (c)

5.2 Crack propagation kinetics

With the crack tip detection method in place, it is possible to plot the evolution of crack size against the number of cycles. The crack size is defined as the length of the segment joins both crack tips (given that cracks tend to follow a straight path outlined by WAAM layers). This evolution is plotted for the 8 detected cracks of sample $SPII$ in Fig.12a. The generated data also allows for the differentiation of the kinetics of both crack tips by plotting the evolution of the half-length defined as the distance between one crack tip and the initiation site. This plot is shown for crack n°1 and n°3 of sample $SPII$ in Fig.12b. A propagation map is also shown (Fig.12c), where the path trajectory of sample $SPII$ cracks, as well as their initiation site and binarized shape are plotted over the initial $\theta^c_{the_a}$ field.

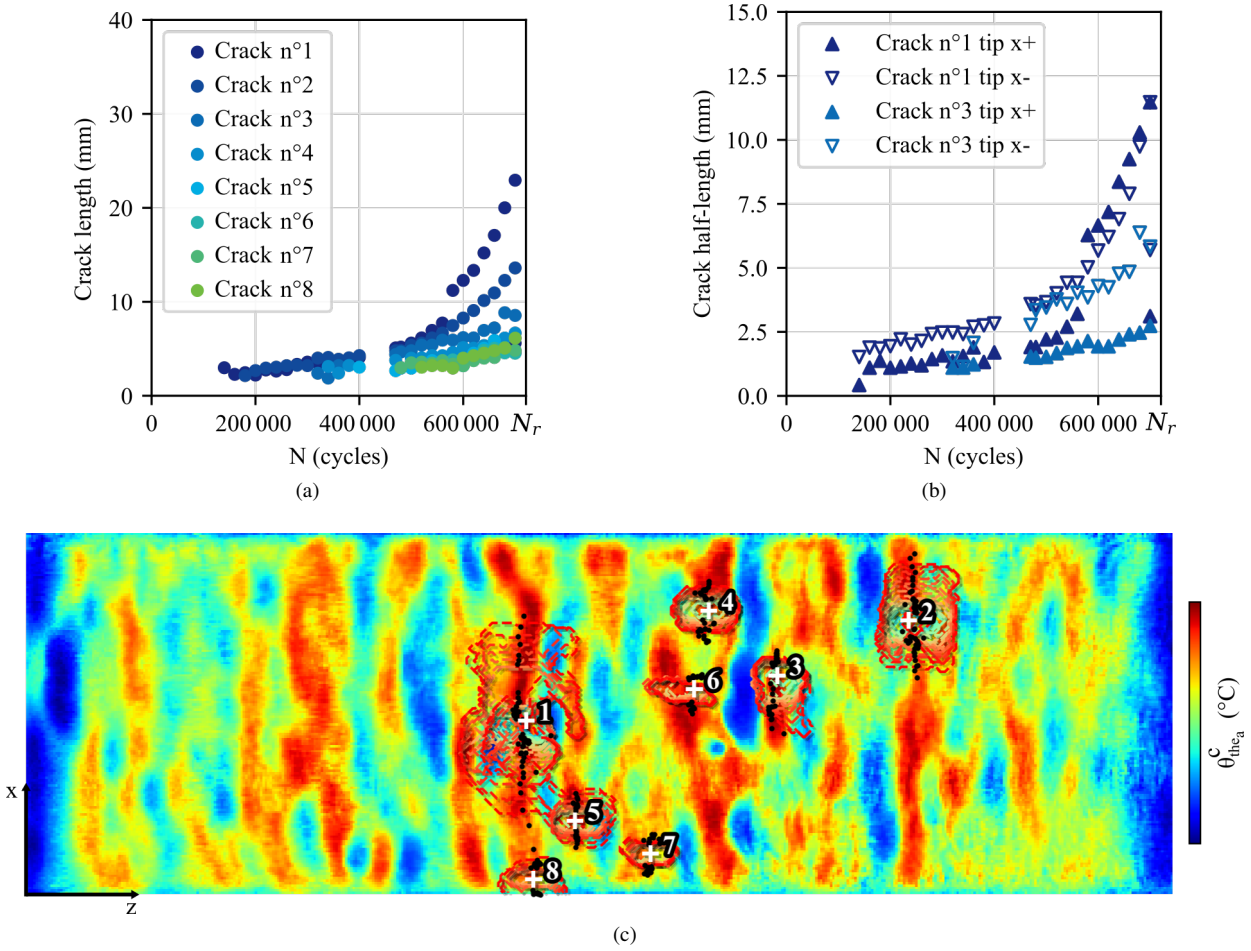

FIGURE 12 – Crack propagation curves in full crack length (a) and half crack length (b) and crack initiation sites, crack tips positions and binary crack shapes on the initial $\theta^c_{the_a}$ field (c)

The propagation curves (Figures 12a and 12b) highlight the existence of a coalescence phenomenon for crack n°1, at the $x+$ crack tip, with a small undetected crack at about 660 000 cycles, resulting in a sudden jump in crack length value. This is also visible on the propagation map (Fig.12c), where a wide space is left between two consecutive crack tips along the x axis in the positive direction.

Crack n°3 is of particular interest on this example, as it shows a very peculiar propagation that is proper to WAAM rough surfaces. Indeed, the crack half-length propagation curve (Fig.12b) highlights an asymmetric crack propagation, where the $x-$ crack tip moves away further from the crack initiation site than does the $x+$ crack tip. On the propagation map (Fig.12c), the $x+$ tip of crack n°3 appears to be stuck in a $\theta^c_{the_a}$ concentration dead-end because of the surface geometry. On the contrary, the dominant crack n°1 is free to propagate in a large and seemingly continuous band of high $\theta^c_{the_a}$, *i.e.*, high stress. It tends to show that the stress concentration induced by the roughness on the surface affects the crack propagation kinetics. It appears that complex propagation scenario can exist on a rough WAAM surface, and that those can be detected, described and characterized through the proposed experimental protocol.

5.3 Dominant cracks analysis

The cracks in samples SPI to $SPVI$ were monitored. In order to characterize the propagation behavior of single cracks on a rough WAAM surface, the dominant crack (the one with the richest propagation data) of each sample is considered. Their propagation curves are plotted in Fig.13a considering a normalized number of cycles.

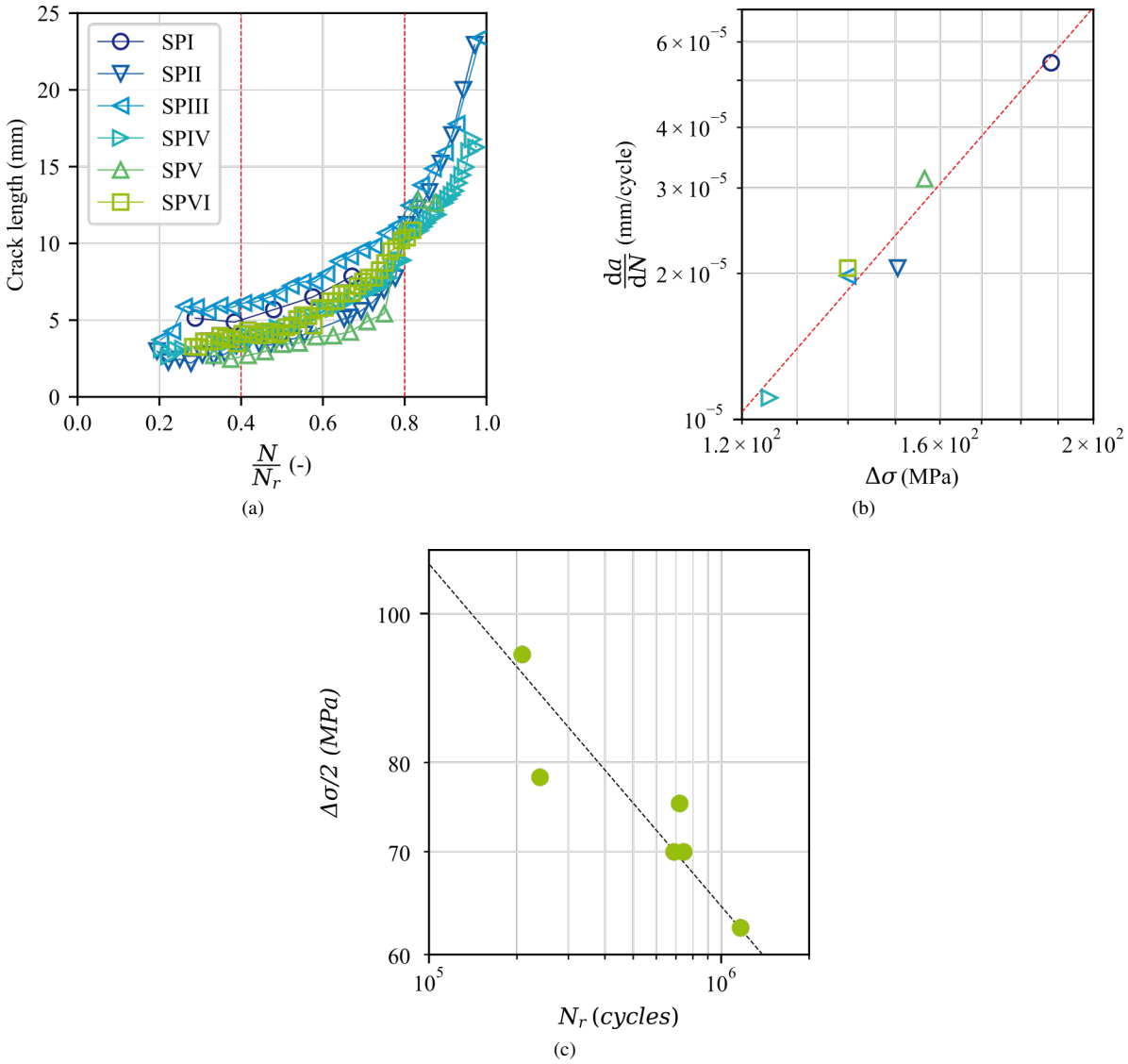

FIGURE 13 – Propagation curves in normalized number of cycles for sample SPI to $SPVI$ (a), corresponding propagation speed between 40% and 80% of the total fatigue life (b) and fatigue tests results of rough WAAM samples SPI to $SPVI$ (c)

In linear fracture mechanics, the crack propagation kinetics can be described using a Paris law

$$\frac{da}{dN} = C_p \Delta K^{m_p}, \tag{17}$$

where a is the crack length, C_p and m_p are material parameters and ΔK is the stress intensity factor range. A generic expression of ΔK is

$$\Delta K = F(a)\, \Delta\sigma \sqrt{\pi a} \tag{18}$$

whereby $F(a)$ is a correction factor to take into account finite thickness and width effects, loading type or even crack shape, and whereby $\Delta\sigma$ is the stress range. Given the propagation data in Fig.13a, for a crack of a few millimeters, between 40% and 80% of the total fatigue life N_r, the propagation speed $\frac{da}{dN}$ appears constant, meaning that $\frac{da}{dN}$ is independent of a. Then, according to the Paris equation (Equation 17), the crack propagation speed $\frac{da}{dN}$ is linear with respect to the stress range $\Delta\sigma$ in log-log scale. By plotting the evolution of the crack propagation speed $\frac{da}{dN}$ determined from the experimental infrared data against the stress range $\Delta\sigma$ for samples

SPI to $SPVI$, it is possible to determine the Paris parameter m_p as the slope of the curve in logarithmic scale (Fig.13b). The value $m_p = 4.2$ is found.

Alternatively, given the fatigue results of samples SPI to $SPVI$, it is possible to plot the number of cycles to failure N_r against the stress range $\Delta\sigma$ in order to determine the Basquin relationship

$$N_r \Delta\sigma^b = B, \tag{19}$$

with b and B material parameters relative to the Basquin law. From the experimental results, plotted in Fig.13c, the value $b = 4.5$ is found. It appears that the Basquin exponent b and the Paris exponent m_p are very close, which is coherent with the experimental observation that the fatigue life of the rough WAAM samples is driven by crack propagation. Moreover, it advocates for the adoption of a crack propagation-based approach in the fatigue life forecast of rough as-built WAAM parts.

6 Summary and conclusions

In this study, an experimental method was presented in order to investigate the effect of process-induced surface roughness of the fatigue performances of bronze-aluminum as-built WAAM samples. On the basis of the experimental results, the following observations were made:

1. Given a discretization of geometries in layers and weld beads, the WAAM process induces a significant surface roughness that is anisotropic. Given a surface sample, an arithmetic roughness R_a of 236 µm was measured in the building direction, and 171 µm in the direction perpendicular to the building direction ;
2. The rough surface characteristic length (layer thickness of about 3mm) is compatible with the applied thermoelastic stress analysis protocol given the considered material and the loading frequency of $f_m = 5$ Hz ;
3. The presence of fatigue cracks of a full-length between 2 and 3 millimeters over a large area can be revealed in the temperature amplitude differential $\Delta\theta^c_{the}$ field. Using an adapted binarization technique, their initiation site can also be determined ;
4. The confrontation of experimental crack initiation sites and the local numerical stress field demonstrates the existence of a non-deterministic relationship, whereby an initiation site necessarily corresponds to a high stress concentration, while a high stress concentration does not necessarily give rise to crack initiation ;
5. A systematic multi-crack initiation is observed, leading to crack interaction phenomena such as obscuration (or shielding) and coalescence ;
6. It is found that at most 35% of the total fatigue life consist of fatigue crack initiation, meaning that the fatigue life of rough WAAM samples is driven by crack propagation ;
7. The fatigue crack propagation of multiple cracks over a large area can be tracked using the proposed image post-processing techniques on the infrared data, allowing for the characterization of the propagation kinetics (following a Paris law for example).

Finally, the presented experimental method has demonstrated its capability in the identification of a full fatigue model based on linear fracture mechanics with a probabilistic aspect (relationship between high-stress zones and crack initiation) that is specific to the process induced roughness.

Acknowledgements

The authors would like to thank Direction Générale de l'Armement (DGA) for its support. This work was completed as part of the Gustave Zédé joint-lab collaborative research between Naval Group and ENSTA Bretagne. Part of this study belongs to the "Self-Heating" ANR - Safran - Naval Group Research Chair (Grant # ANR-20-CHIN-0002) involving Safran Companies, Naval Group, ENSTA Bretagne (IRDL) and Institut Pprime.

AUTHORS STATEMENT FOR PUBLICATION

Manuscript title: Thermometric investigations for the characterization of fatigue crack initiation and propagation in Wire and Arc Additively Manufactured parts with as-built surfaces

Corresponding author's full name: Lorenzo Bercelli

I declare that all listed authors have made substantial contributions to all of the following three parts of the manuscript: research design, or acquisition, analysis or interpretation of data; drafting the paper or revising it critically; approving the submitted version. I also declare that no-one who qualifies for authorship has been excluded from the list of authors.

I declare that I have communicated with all other authors and I have obtained their approval for the final version to be published.

Date (dd/mm/yyyy)

07/04/2022

Corresponding author's signature

References

1. Ivántabernero, Paskual A, Álvarez P, Suárez A. Study on Arc Welding Processes for High Deposition Rate Additive Manufacturing. *Procedia CIRP* 2018 ;68: 358–362.
2. Yadollahi A, Mahtabi MJ, Khalili A, Doude HR, Newman JC. Fatigue life prediction of additively manufactured material: Effects of surface roughness, defect size, and shape. *Fatigue Fract. Eng. Mater. Struct.* 2018 ;41: 1602–1614.
3. Pegues JW, Shamsaei N, Roach MD, Williamson RS. Fatigue life estimation of additive manufactured parts in the as-built surface condition. *Material Des. Process. Commun.* 2019 ;1: e36.
4. Vayssette B, Saintier N, Brugger C, El May M, May ME. Surface roughness effect of SLM and EBM Ti-6Al-4V on multiaxial high cycle fatigue. *Theor. Appl. Fract. Mech.* 2020 ;108: 102581.
5. Koutiri I, Pessard E, Peyre P, Amlou O, De Terris T. Influence of SLM process parameters on the surface finish, porosity rate and fatigue behavior of as-built Inconel 625 parts. *J. Mater. Process. Technol.* 2018 ;255: 536–546.
6. Mumtaz KA, Hopkinson N. Selective Laser Melting of thin wall parts using pulse shaping. *J. Mater. Process. Technol.* 2010 ; 210: 279–287.
7. Bartsch H, Kühne R, Citarelli S, Schaffrath S, Feldmann M. Fatigue analysis of wire arc additive manufactured (3D printed) components with unmilled surface. *Structures* 2021 ;31: 576–589.
8. Xia C, Pan Z, Polden J, Li H, Xu Y, Chen S. Modelling and prediction of surface roughness in wire arc additive manufacturing using machine learning. *J. Intell. Manuf.* 2021 ;.
9. Murakami Y, Endo M. Effects of defects, inclusions and inhomogeneities on fatigue strength. *Int. J. Fatigue* 1994 ;16: 163–182.
10. Wycisk E, Solbach A, Siddique S, Herzog D, Walther F, Emmelmann C. Effects of defects in laser additive manufactured Ti-6Al-4V on fatigue properties. *Phys. Procedia* 2014 ;56: 371–378.
11. Newman Jr J. FASTRAN II - A fatigue crack growth structural analysis program, 1992.
12. Yadollahi A, Shamsaei N, Thompson SM, Elwany A, Bian L. Effects of building orientation and heat treatment on fatigue behavior of selective laser melted 17-4 PH stainless steel. *Int. J. Fatigue* 2017 ;94: 218–235.
13. Sanaei N, Fatemi A. Defects in additive manufactured metals and their effect on fatigue performance: A state-of-the-art review. *Prog. Mater. Sci.* 2021 ;117: 100724.
14. Sanaei N, Fatemi A. Defect-based fatigue life prediction of L-PBF additive manufactured metals. *Eng. Fract. Mech.* 2021 ;244: 107541.
15. Masuo H, Tanaka Y, Morokoshi S, Yagura H, Uchida T, Yamamoto Y, et al. Effects of Defects , Surface on Fatigue of Ti-6Al-4V manufactured by Additive Manufacturing. *Procedia Struct. Integr.* 2017 ;19–26.
16. Mettu SR, Shivakumar V, Beek JM, Yeh F, Williams LC, Forman R, et al. NASGRO 3.0 - A Software For Analyzing Aging Aircraft. In *The Second Joint NASA/FAA/DoD Conference on Aging Aircraft*. 1999 .
17. Vayssette B, Saintier N, Brugger C, El May M, Pessard E. Numerical modelling of surface roughness effect on the fatigue behavior of Ti-6Al-4V obtained by additive manufacturing. *Int. J. Fatigue* 2019 ;123: 180–195.
18. Crossland B. Effect of large hydrostatic pressures on the torsional fatigue strength of an alloy steel. In *International conference on fatigue of metals*. 1956 12.
19. Samadian K, Waele WD, de Waele W. Fatigue crack growth model incorporating surface waviness for wire+arc additively manufactured components. *Procedia Struct. Integr.* 2020 ;28: 1846–1855.
20. Kitsunai Y, Sasaki T, Honda T. Determination of stress concentration factors and stress intensity factors by means of thermoelastic effect. *Comput. Aided Assess. Control. Localized Damage - Proc. Int. Conf.* 1996 ;13: 751–758.
21. Sakagami T, Mizokami Y, Shiozawa D, Izumi Y, Moriyama A. TSA based evaluation of fatigue crack propagation in steel bridge members. *Procedia Struct. Integr.* 2017 ;5: 1370–1376.
22. Meneghetti G, Ricotta M, Pitarresi G. Infrared thermography-based evaluation of the elastic-plastic J-integral to correlate fatigue crack growth data of a stainless steel. *Int. J. Fatigue* 2019 ;125: 149–160.
23. Boussattine Z, Ranc N, Palin-Luc T. About the heat sources generated during fatigue crack growth: What consequences on the stress intensity factor ? *Theor. Appl. Fract. Mech.* 2020 ;109: 102704.
24. Carteron L, Doudard C, Calloch S, Levieil B, Beaudet J, Bridier F. Naval welded joints local stress assessment and fatigue cracks monitoring with quantitative thermoelastic stress analysis. *Theor. Appl. Fract. Mech.* 2020 ;110: 102792.

25. De Finis R, Palumbo D, Carolo FD, Ricotta M, Meneghetti G, Galietti U. Crack tip position evaluation and Paris' law assessment of a propagating crack by means of temperature-based approaches. *Procedia Struct. Integr*. 2021 ;39: 528–545.
26. Queguineur A, Marolleau J, Lavergne A, Rückert G. Evaluation of tandem controlled short-circuit GMAW for improved deposition in additive manufacture of large Nickel Aluminium Bronze naval components. *Weld. World* 2020 ;64: 1389–1395.
27. Qiu Z, Wu B, Zhu H, Wang Z, Hellier A, Ma Y, et al. Microstructure and mechanical properties of wire arc additively manufactured Hastelloy C276 alloy. *Mater. Des*. 2020 ;195: 109007.
28. Horgar A, Fostervoll H, Nyhus B, Ren X, Eriksson M, Akselsen OM. Additive manufacturing using WAAM with AA5183 wire. *J. Mater. Process. Technol*. 2018 ;259: 68–74.
29. Bercelli L, Moyne S, Dhondt M, Doudard C, Calloch S, Beaudet J. A probabilistic approach for high cycle fatigue of Wire and Arc Additive Manufactured parts taking into account process-induced pores. *Addit. Manuf*. 2021 ;42.
30. Vollmer M, Möllmann KP. *Infrared Thermal Imaging*, Weinheim, Germany: Wiley-VCH Verlag GmbH and Co. KGaA2017.
31. Breitenstein O, Warta W, Langenkamp M. *Lock-in Thermography - Basics and Use for Evaluating Electronic Devices and Materials*, Berlin: Springer2010.
32. Brémond P, Potet P, Systems CI, Croissy-beaubourg-france-pierrebremondcedip infraredcom BGBF. Lock-In Thermography : A tool to analyse and locate thermo-mechanical mechanisms in materials and structures. In *Proceedings SPIE 4360, Thermosens XXII*, vol. 4360. 2001 560–566.
33. Sakagami T. Remote nondestructive evaluation technique using infrared thermography for fatigue cracks in steel bridges. *Fatigue Fract. Eng. Mater. Struct*. 2015 ;38: 755–779.
34. Stanley P. Beginnings and early development of thermoelastic stress analysis. *Strain* 2008 ;44: 285–297.
35. Lemaitre J, Chaboche JL. *Mechanics of Solid Materials*, Cambridge University Press1990.
36. Le Saux V, Doudard C. Infrared Physics and Technology Proposition of a compensated pixelwise calibration for photonic infrared cameras and comparison to classic calibration procedures : Case of thermoelastic stress analysis. *Infrared Phys. Technol*. 2017 ; 80: 83–92.

Highlights

— Fatigue cracks on as-built WAAM surfaces can be monitored via infrared thermography
— Fatigue life of as-built WAAM samples is dominated by a crack propagation phase
— The link between surface stress concentration and crack initiation in non-deterministic